JOURNAL OF THERMOPHYSICS AND HEAT TRANSFER
Vol. 20, No. 1, January–March 2006

Analysis of Apollo Command Module Afterbody Heating Part I: AS-202

Michael J. Wright*
NASA Ames Research Center, Moffett Field, California 94035
Dinesh K. Prabhu†
ELORET Corporation, Sunnyvale, California 94087
and
Edward R. Martinez‡
NASA Ames Research Center, Moffett Field, California 94035

Computational-fluid-dynamics simulations are performed to simulate the wake flow and afterbody heating environment of the Apollo AS-202 command module reentry. Fifteen three-dimensional simulations that cover the majority of the high-heating portion of the flight are computed. Computed surface oil flow plots predict that the flow remained attached on the windward side of the afterbody throughout the entry. The computed heat transfer generally agrees well with the flight data and is within the estimated ±20% uncertainty for 15 of the 19 functional calorimeters on the conical afterbody over most of the entry. Heat transfer is generally overpredicted in the attached flow region during the low-Reynolds-number portion of the trajectory, possibly because of noncontinuum effects. Predicted heating at two calorimeters located near the separation line clearly shows jumps where the flow separates and reattaches as a function of time. This behavior is also seen in the flight data, indicating that the computational results are accurately predicting not only heating levels but separated flow extent as well. The worst agreement between the computations and the flight data occurs near the rear apex of the command module. The reason for this disagreement is not known at this time, but might be partially caused by geometric differences between the apex as modeled in this work and the flight vehicle. The effects of sideslip are explored and found to be minor at all but four calorimeter locations.

Nomenclature

L	=	running length, m
M	=	Mach number
q	=	heat transfer, W/cm^2
R	=	radius, m
T	=	temperature, K
t	=	time, s
u	=	axial component of velocity vector, m/s
V	=	velocity, m/s
x	=	length from nose, cm
α	=	angle of attack, deg
β	=	sideslip angle, deg
γ	=	flight-path angle, deg
ε	=	emissivity
θ	=	circumferential angle, deg
μ	=	kinematic viscosity, Pa · s
ρ	=	density, kg/m^3

Subscripts

D	=	body diameter
e	=	boundary-layer edge
GLL	=	gradient-length local
tr	=	transition
θ	=	momentum thickness
∞	=	freestream

Presented as Paper 2004-2468 at the Thermophysics, Portland, OR, 1 June 2004; received 1 February 2005; revision received 11 April 2005; accepted for publication 12 April 2005.

*Senior Research Scientist, Reacting Flow Environments Branch, MS 230-2. Senior Member AIAA.
†Senior Research Scientist, Reacting Flow Environments Branch, MS 230-2. Associate Fellow AIAA.
‡Senior Research Engineer, Thermo-Physics Facilities Branch, MS 229-3.

I. Introduction

AN improved understanding of the aerothermal environment on the afterbody of planetary entry vehicles is important for future missions. Current design practice typically imposes a large uncertainty on computed afterbody heating rates. This large uncertainty can have significant impact on the afterbody thermal protection system (TPS), affecting the material selected for a given mission as well as the final system mass. Unnecessary conservatism in the afterbody heat-shield design will also shift the center of gravity of the vehicle backward, reducing stability and possibly necessitating ballast in the nose. A primary reason for this uncertainty is a perceived lack of data for code validation. Ground-test data are typically complicated by sting interference effects, and flight data are extremely limited. Therefore, it is critical to understand and fully utilize of the flight data that are available to improve the next generation of Earth and planetary entry vehicles and to assess the need for additional flight testing and computational-fluid-dynamics (CFD) model development.

The Apollo program spent considerable resources on testing to quantify the aerothermal environment around the reentering command module. Ground-based tests were conducted in low-enthalpy wind tunnels, shock tunnels, and free-flight facilities,[1–6] the data from which were used to build engineering-fidelity predictions of the expected flight heating rates. Two flight tests (Fire-I and Fire-II)[7,8] were then conducted primarily to measure radiative heating. Once the Apollo entry vehicle design was determined, two flight tests of the actual command module (AS-201 and AS-202) were conducted at orbital velocities,[9] and two flights (Apollo 4 and 6) were conducted at superorbital velocities.[10] Although AS-201 did not carry an onboard inertial measurement unit (IMU), one was carried during the other three flights, which enabled an accurate reconstruction of the flight trajectory and vehicle orientation as a function of time. The range of entry velocities and angles of attack

Table 1 Entry conditions for the Apollo command module flight tests

Flight designation	V, km/s	α, deg	γ, deg	Max decel, g	Theoretical max heating, W/cm^2
AS-201	7.67	20	−8.6	14.3	186
AS-202	8.29	18	−3.5	2.4	91
Apollo 4	10.73	25	−5.9	4.6	237
Apollo 6	9.60	25	−6.9	7.3	488

during these flights was sufficient to span multiple flow regimes, from laminar to fully turbulent flow, as well as a regime with minimal TPS-fluid interaction to one with strong pyrolysis gas injection and char formation. Table 1, reproduced from Ref. 11, lists the relevant entry conditions for each of the four Apollo test flights. In Table 1, V is the entry velocity at atmospheric interface, α is nominal the angle of attack, and γ is the flight-path angle. The maximum theoretical heating rate in Table 1 was determined by engineering correlations for a spherical stagnation point.

In a previous paper,[12] we compared CFD predictions of afterbody heating to flight data for the Fire-II flight experiment. The computations generally agreed with flight data to within the experimental uncertainty, and areas of disagreement were explainable by unmodeled TPS material response. Those results demonstrated the ability of modern computational methods to accurately compute the afterbody heating environment of a laminar axisymmetric flow without significant material response. The next steps are to examine flight data for vehicles at angle of attack, with the addition of significant material response and turbulent transition. A prime data source for this purpose is the four Apollo flight tests. Many previous researchers have studied forebody convective and radiative heating results from these flights,[13,14] but to our knowledge the afterbody heating and pressure data have not been previously examined using modern CFD.

In this paper we take the first step at simulating the afterbody heating environment for the Apollo command module, concentrating on the orbital AS-202 mission. The AS-202 flight was chosen as the starting point for such an analysis for several reasons. First, as discussed earlier this flight was the first with an onboard IMU, which permits an accurate trajectory reconstruction. Also, the AS-202 mission had the lowest afterbody heat fluxes of the four flights, and the recovered capsule indicated that the afterbody suffered little charring during entry. Therefore analysis of this mission can be used to first establish the ability to predict afterbody heating levels of a lifting vehicle in the absence of ablation before attempting to simulate the more complex flows.

II. Command Module Geometry

Figure 1 is a schematic drawing of the Apollo command module outer mold line (OML) as modeled in this work. The capsule was designed to enter the atmosphere at an angle of attack of approximately 25 deg via an offset center of gravity, thereby achieving a lift-to-drag ratio of about 0.3. Note that in the Apollo-era literature the spherical-section aeroshell, which points into the oncoming flow, is labeled the aft section because of the position of the astronauts. However, in this paper we use the modern (flow-oriented) nomenclature and will refer to the spherical section as the forebody and the conical section as the afterbody. The command module forebody consists of a spherical section with a radius of curvature of 4.694 m. The shoulder radius is 0.196 m or 10% of the radius of the body. The afterbody consists of a 33-deg conical section, blunted to a 0.231-m radius at the aft end. The maximum diameter of the capsule is 3.912 m, and the axial length, including the TPS material, is 3.431 m.

In the early days of the Apollo program, the OML of the command module underwent frequent design changes, and there is considerable discrepancy in the literature among values for the radii of the shoulder and the blunted rear of the capsule. The values used in this paper are consistent with the instrument locations and geometry description in Ref. 9. The OML as modeled in this work is a simplification of the actual geometry, neglecting the umbilical housing,

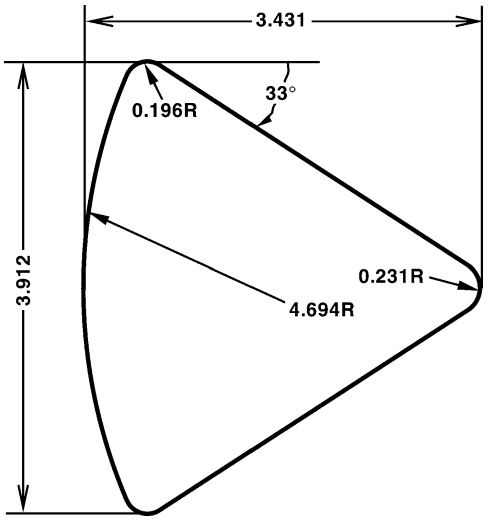

Fig. 1 Schematic drawing of the outer mold line of AS-202 capsule as modeled in this work. All dimensions in meters.

scimitar antennas, viewing windows, and reaction-control-system (RCS) thrusters on the leeside. The scimitar antennas and umbilical housing in particular are sizable protrusions (see next section and dimensions in Ref. 15) that will certainly alter the flowfield in their vicinity. In addition, the spherical-section heat shield on the forebody of the capsule was canted at 0.195 deg from the structural centerline, creating a small asymmetry in the OML.[15] Also, because of the variable thickness of the TPS material applied to the aeroshell (see the following), the effective shoulder radius varied from the windward to the leeward side of the vehicle. Hillje[15] gives these radii to be 0.19 m on the windward centerline and 0.18 m on the leeward centerline, respectively, for the command module flown during the AS-202 mission (CM-011). The slight asymmetries caused by heat-shield cant and shoulder radius variation are not modeled in this work.

The outermost layer of the TPS on the entire aeroshell consisted of Avcoat 5026/39G, an ablator developed for the Apollo program. The Avcoat material was injected into a phenolic honeycomb matrix, which was bonded to a stainless-steel substructure.[16] Avcoat 5026/39G was an epoxy resin reinforced with quartz fibers and lightened with phenolic microballoons to obtain a final density of 244.6 kg/m^3 (Ref. 17). The final ablator thickness was variable according to the predicted aerothermal environment and ranged from 6.86 cm on the windward side of the spherical forebody to 1.79 cm near the rear apex of the conical afterbody.[16] The afterbody of the capsule was painted with a titanium-oxide (white) paint for cosmetic reasons and also to act as a moisture barrier during prelaunch storage.

III. Flight Instrumentation

A total of 12 pressure transducers and 12 calorimeters were placed on the forebody of the aeroshell. Usable pressure data were obtained from 10 of the 12 pressure transducers; however, none of the forebody slug calorimeters, which were designed specifically for the Apollo program, produced usable data during either the AS-201 or AS-202 flights.[9] These calorimeters were redesigned before the Apollo 4 and 6 flights.[10]

Twenty-three calorimeters were placed on the afterbody. Of these, 19 functioned properly during the AS-202 mission. Figure 2 shows the locations of the surface-mounted calorimeters on the afterbody aeroshell for both the AS-201 and AS-202 test flights, and Table 2 gives the location of each calorimeter in terms of the coordinate system defined in Fig. 2. In this coordinate system, x is measured from the nose of the vehicle to the apex, and θ is the circumferential angle. Here $\theta = 90$ deg lies along the positive z axis and corresponds to the windward centerline assuming no sideslip, and $\theta = 270$ deg corresponds to the leeward centerline. The calorimeter locations

Table 2 Afterbody calorimeter locations for AS-202

ID[a]	X,[b] cm	θ,[b] deg	Range, W/cm^2
——	72.6	93.7	0–114
a	120.8	85.3	0–57
b	169.8	92.0	0–57
c	205.6	115.0	0–57
d	294.8	83.4	0–57
e	343.1	Apex	0–28
f	69.5	138.0	0–57
g	161.5	142.8	0–28
h	54.5	178.5	0–28
i	54.5	270.0	0–11.4
j	94.1	178.6	0–28
k	157.6	177.5	0–28
l	228.8	182.9	0–28
m	106.8	215.3	0–11.4
n	69.5	225.5	0–11.4
——	205.6	191.3	0–28
o	136.6	229.8	0–11.4
p	152.6	234.0	0–28
q	184.3	276.4	0–28
r	205.6	267.8	0–28
s	294.8	265.0	0–28
——	74.1	253.0	0–28
——	88.0	253.0	0–57

[a]Corresponds to Fig. 17 in Ref. 9. Those without letters were nonfunctional during AS-202.
[b]Refer to Fig. 2 for coordinate system definition.

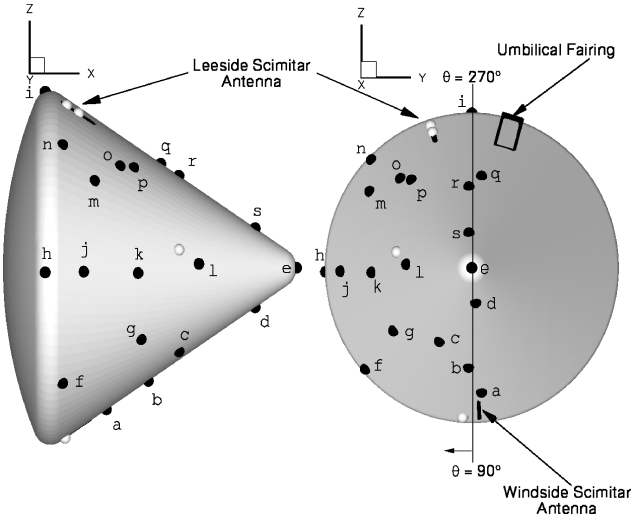

Fig. 2 Locations of calorimeters on AS-202 conical afterbody. White symbols indicate inoperative instruments. Letters correspond to the ID in Table 2.

given in Ref. 9 assumed that $x = 0$ was at the vehicle nose before the application of the ablative TPS material. Therefore all x coordinates given in Table 2 were adjusted from those in Ref. 9 by the 5.23-cm ablator thickness at the nose.[16] Those calorimeters that provided usable data during the entry are labeled in Table 2 with a letter code that matches that used in Fig. 17 of Ref. 9.

The afterbody calorimeters were designed to measure heating rates of less than 58 W/cm^2. A schematic diagram is given in Ref. 9. These calorimeters are essentially Gardon gauges,[18] which are in common use for measurement of steady-state radiation and convective heat flux. The gauge is explicitly designed to work in convective stagnation flows and is calibrated assuming that the peak temperature is at the center of the 0.66-cm-diam constantan foil disk. A potentially significant source of error is introduced when the gauge is used in a shear flow moving parallel to the foil surface, causing the peak foil temperature to deviate from its center. One way to alleviate this error source is to use a larger diameter foil than required for the heating rate. In shear flow applications the standard guidance[19] is to use a gauge that has a maximum measurable heating rate of about 20 times the expected value. Comparing the ranges for each gauge as listed in Table 2 with the measured flight heating levels in Ref. 9, we note that this guidance was followed for all gauges except h and i. The gauge under laboratory conditions can produce a minimum uncertainty of ±3%, but under flight conditions in shear flow an uncertainty of approximately ±20% is reasonable.[20] Because measurement uncertainties on the flight data were not given in the literature, a value of ±20% will be assumed in this work.

Twenty-four pressure transducers were also used on the afterbody of the spacecraft. However, none of the 22 pressure transducers on the conical afterbody and only one of the two on the shoulder detected a measurable pressure rise until just prior to parachute deployment. Therefore no meaningful comparisons to flight pressure data can be made.

Also shown in Fig. 2 is the approximate position of the two scimitar antennas and the umbilical fairing, which are not modeled in the current work. The antennas had a semicircular profile with a width of less than 2 cm and a maximum height of about 20 cm (Ref. 15). The leeward antenna survived intact, but the antenna on the wind side was destroyed during the entry. Because of their small profile, it is likely that their effect on the flowfield would be local, and therefore eliminating them from the OML used in this work should not have a major impact on the results. The one exception to this might be the heating data from calorimeter a, which is located immediately downstream of the windward antenna. The fidelity of the data from calorimeter a will be explored in the comparison to experimental data given next. The umbilical housing had a larger profile, but was on the side of the afterbody opposite the majority of the calorimeters and therefore should not have a major influence on the results presented here.

Finally, although afterbody radiometers were not used on AS-202, two radiometers were placed on the conical afterbody during the Apollo 4 and 6 flights. Although both were determined to be functional, neither measured any signal during the heating pulse, indicating that radiative heating to the conical section was negligible.[11] Because the reentry environment for the AS-202 flight was much less severe than that for Apollo 4 and 6, we can surmise that there was zero radiative heating to the afterbody for these flights.

IV. Aerodynamics and Trajectory Reconstruction

Flight aerodynamics were reported by Hillje,[15] as reconstructed from the onboard IMU. The command module entered the atmosphere at 8.3 km/s at 4390 s after launch on a shallow flight-path angle of –3.53 deg and a nominal angle of attack of 18 deg. AS-202 was the first Apollo mission with an active guidance system; thus, one of the primary flight objectives was to test the guidance and RCS. Therefore a roll reversal was planned between 4410 and 4480 s to orient the capsule in a lift-up position and enable a "skip" or lofting phase during the entry. Figure 3 shows the reconstructed altitude and velocity as a function of time.[15] As seen in Fig. 3, a

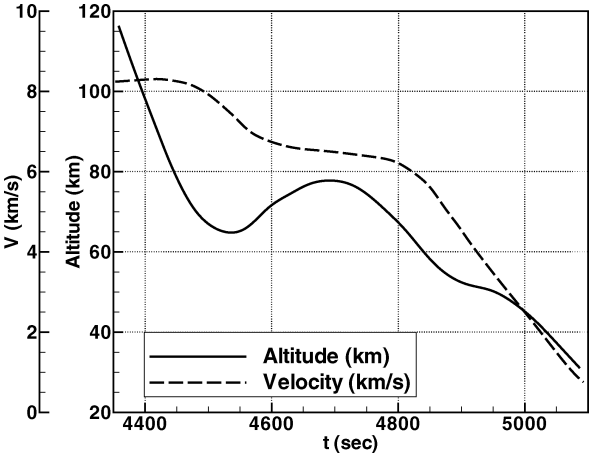

Fig. 3 Altitude and velocity as a function of time from launch for AS-202.

local minimum in altitude was achieved at about 4520 s, followed by the skip phase, which lasted until a local maximum in altitude was achieved at approximately 4690 s. After a second roll reversal, the capsule continued its descent. This skipping trajectory resulted in two distinct heating pulses during the entry. The angle of attack remained within ±0.5 deg of nominal during most of the entry, but began to increase at about 4900 s, reaching a value of about 20 deg by 5000 s after launch. Although the vehicle was not intended to have any sideslip during the entry, the flight aerodynamics data indicate that a nearly constant sideslip angle of about 2.5 ± 0.5 deg was present.[15] This paper will examine the impact of sideslip on the afterbody heat-transfer distribution.

Atmospheric conditions along the entry trajectory were obtained via sounding rockets to an altitude of 55 km. The sounding rocket data were then extrapolated vertically to entry interface using standard hydrostatic relations.[21] Atmospheric density and temperature as a function of time for AS-202 are given in Ref. 9.

V. Methodology

The flowfield computations are performed using the CFD code DPLR.[12,22] DPLR is a parallel multiblock finite volume code that solves the reacting Navier–Stokes equations including finite-rate chemistry and the effects of thermal nonequilibrium. The Euler fluxes are computed using a modified (low-dissipation) form of Steger–Warming flux vector splitting,[23] with third-order spatial accuracy obtained via monotonic upstream schemes for conservation law (MUSCL) extrapolation.[24] Viscous fluxes are computed to second-order accuracy using a central difference approach. DPLR has been used previously on several planetary entry simulations.[12,25,26] At the entry velocities considered in this work, the level of flowfield ionization will be small; forebody calculations near the peak heating point indicated ionization levels of less than 0.3%. Therefore a five-species (N_2, O_2, NO, N, O) five-reaction finite-rate air chemistry model is used.[27,28] The flow is assumed to be in thermal nonequilibrium, according to the two-temperature model of Park.[29] Vibrational relaxation is modeled using a Landau–Teller formulation, where relaxation times are obtained from Millikan and White,[30] assuming simple harmonic oscillators.

Viscous transport and thermal conductivity are modeled using the mixing rules presented by Gupta et al.,[31] which have been shown to be reasonable approximations of the more accurate Chapman–Enskog relations in this flow regime.[32,33] The self-consistent effective binary diffusion method is used to compute the species diffusion coefficients.[34] This method allows for the variations in species diffusion coefficients to be accurately modeled without sacrificing the requirement that the diffusion velocities sum identically to zero. Postflight interpretation of the heating data indicated that the flowfield on the conical afterbody remained entirely laminar prior to the atmospheric skip maneuver ($t < 4800$ s) (Ref. 9). The windward side of the afterbody was assumed to have transitioned to turbulence after the skip[9]; however, the leeward (separated) side apparently remained laminar. The majority of the results presented in this work assume laminar flow; however, the possibility of turbulent transition, particularly after the skip maneuver, is explored. The impact of turbulence on heating levels for the attached flow region of the afterbody is examined using Menter's shear-stress-transport (SST) two-equation turbulence model[35] with corrections for compressible flows. This model was shown[36] to give reasonable results in hypersonic separated flow regions. The turbulent solutions were run with a turbulent Schmidt number of 0.5.

Surface catalysis is modeled using a diffusion-limited approach.[29] The surface is assumed to be fully catalytic to N_2 and O_2 recombination, which should be reasonable for the hydrocarbon resin-based Avcoat material. At very high heat fluxes the quartz fibers in the material would begin to melt, which would reduce the effective surface catalycity, but this would not have occurred at the relatively low heat fluxes measured on the conical afterbody during this flight. The afterbody surface was initially coated with a titanium dioxide paint, which likely had a fairly low catalycity. However, this paint would have burned away early in the entry, exposing the highly catalytic Avcoat TPS to the flow. The asymptotic calorimeters on the aft shell were surface mounted and thus exposed to the flow. Therefore it is possible that the calorimeters had a different catalycity than the underlying TPS, which could lead to catalytic heating jumps at the sensor location. However, in this case the calorimeter surface should be nearly fully catalytic and thus should have blended well with the catalytic TPS. The surface temperature is computed assuming radiative equilibrium with a constant emissivity of 0.85, a value typical of carbonaceous ablators. The foil disk of the calorimeter surface would possibly have a lower emissivity than the Avcoat, but because heat flux is a weak function of emissivity this difference was not considered to be important. The effects of varying surface catalysis and emissivity on the computed heat transfer will be explored in the following section.

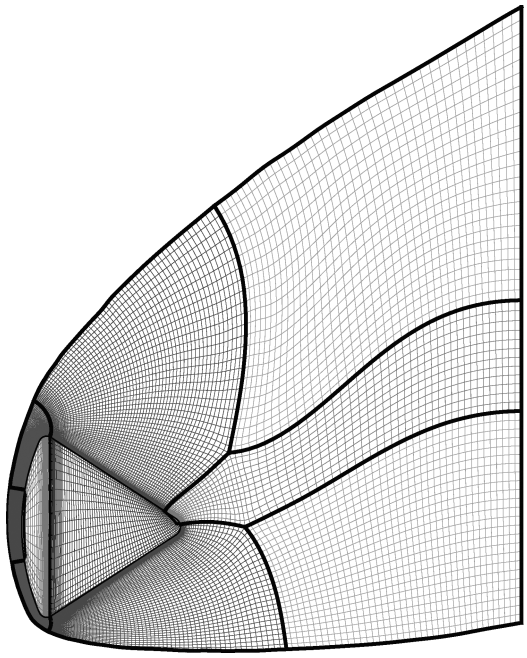

Fig. 4 Grid topology used in this work. Every other point shown in each direction of the pitch plane and body surface.

Shock-layer radiation is neglected, because of the low entry velocity and the fact that radiometers on the higher velocity Apollo 4 and 6 entries failed to detect any radiation signal on the afterbody.[11] Material ablation and thermal response are also neglected, as their effects on computed surface heating should be negligibly small for the low heat fluxes observed on the afterbody of the AS-202 flight.

Wake flows are sensitive to the details of the volume grid construction, and it is important to generate a grid that is well aligned to anticipated flow features. In particular, it is extremely important that the grid have sufficient points in the shoulder region to capture the rapid expansion and accurately predict the flow separation point and the angle of the resulting shear layer.[37] There must also be sufficient points in the separated flow region to resolve the vortical structure and the wake compression, or neck. The baseline grid topology for this work (Fig. 4) consists of five grid blocks and is constructed to permit local refinement of the shoulder region and the wake core region while maintaining point matching at every block interface. The solution adaptive grid code (SAGe)[38] is used to tailor the outer boundary of the grid to the shock wave. A grid-resolution study is performed to determine the final density requirements; the results are reported in the following section.

VI. Results

Full three-dimensional CFD solutions are obtained for 15 points along the trajectory, with freestream conditions listed in Table 3. The solutions range from 4455 to 4900 s after launch, with nine of the points concentrated in the first heat pulse ($t = 4455$ to 4700 s). The second heat pulse ($t = 4750$ to 5100 s) is explored in less detail primarily because of the number of RCS events during this time period,

Table 3 AS-202 trajectory points and freestream conditions

Time,[a] s	Alt., km	Re_D[b]	V, km/s	M	ρ_∞, kg/m^3	T_∞, K	α, deg	β, deg
4455	76.8	7.5×10^4	8.24	28.6	$3.38e{-5}$	205	18.2	2.0
4475	71.3	1.8×10^5	8.15	27.6	$8.76e{-5}$	217	17.9	2.5
4500	70.0	3.0×10^5	7.92	26.2	$1.52e{-4}$	227	17.8	2.5
4510	66.0	3.2×10^5	7.80	25.6	$1.69e{-4}$	230	17.8	2.5
4530	64.9	3.4×10^5	7.53	24.5	$1.84e{-4}$	234	17.9	2.5
4560	66.0	2.7×10^5	7.07	23.2	$1.53e{-4}$	231	18.1	2.5
4600	71.6	1.3×10^5	6.74	22.9	$7.19e{-5}$	215	18.3	2.5
4650	76.2	5.7×10^4	6.56	22.8	$3.24e{-5}$	206	18.5	2.0
4700	77.2	4.3×10^4	6.49	22.7	$2.45e{-5}$	203	18.5	2.0
4750	74.5	7.6×10^4	6.39	22.0	$4.50e{-5}$	210	18.4	2.0
4800	67.3	2.1×10^5	6.21	20.5	$1.37e{-4}$	227	18.4	2.0
4825	62.9	3.5×10^5	5.97	19.2	$2.81e{-4}$	239	18.3	2.0
4850	58.2	5.3×10^5	5.62	17.6	$4.14e{-4}$	252	18.3	2.5
4875	54.6	6.9×10^5	5.07	15.6	$6.16e{-4}$	262	18.4	2.5
4900	52.4	7.6×10^5	4.35	13.2	$8.00e{-4}$	268	18.6	2.5

[a]Seconds after launch. [b]Freestream Reynolds number based on body diameter.

which make the data from many of the calorimeters more difficult to interpret, and the fact that the separated flow becomes unsteady late in the flight. Although the wake structure becomes more complex with increasing Reynolds number, the computations indicate that the flow remains steady until about $t = 4850$ s ($Re_D = 5.3 \times 10^5$), at which point the vortices begin to oscillate, leading to unsteady wake flow. The flowfield in the attached portion of the afterbody remains steady throughout the entry. Most of the cases are run assuming bilateral symmetry; the effects of the small sideslip angle were neglected. This approximation should be reasonable for most of the calorimeter locations, but it can have a significant influence in certain areas. To quantify the impact of neglecting the sideslip angle, a single computation at $t = 4500$ s is performed, which included yaw. The results are discussed next.

The calculations are performed on a 1.5-million-point grid (see next section) and require approximately 15–20 h on 16 CPUs of a cluster of dual-processor 2-GHz Xeon machines to reach a steady-state solution (defined as nine orders of magnitude fall in the L2norm density residual combined with visual inspection of the time evolution of afterbody heat transfer).

A. Grid Resolution

The baseline grid for this work consists of 10,000 surface points, with clustering in the shoulder region, and 1.5 million volume points on a 180-deg circumferential distribution. Grid resolution is confirmed by independently varying the point density in each of the three grid directions (streamwise, normal, and circumferential). Solutions are obtained on multiple volume grids to ensure that the final baseline grid density is sufficient to ensure grid independence. Based on previous work,[12,37] the most critical area to resolve is the shoulder region, where the flow separates and the shear layer forms. Therefore, most of the streamwise refinement was confined to this area. Figure 5 shows the computed heat transfer on the afterbody in the pitch plane for five separate computations at $t = 4510$ s, showing the impact of grid refinement in the streamwise (axial) and normal directions. The solution labeled "baseline" is computed on the 1.5-million-point grid just described. The solutions labeled "CA1" and "CA2" are coarsened in the streamwise direction from the baseline by 30 and 20%, respectively. The solution labeled "FA" is refined in the streamwise direction by 20%. The solution labeled "FN" is refined in the normal direction by 50%. As expected, streamwise distribution at the shoulder is by far the most important metric to ensure a grid-resolved solution. On the coarsest grid (CA1) the wake structure has not formed correctly, leading to differences in heat transfer of about 10% on the attached side and over 100% in the separated flow region. The solution on grid "CA2" of the wake structure is better resolved, but differences in heating of up to 5% on the windside flow and 15% on the leeside are still seen. The solution with fine streamwise spacing (FA) is almost identical to the baseline except near the apex, where differences of about 5% are still present. By contrast, a 50% increase in the normal and a 25% increase in the circumferential (not shown) point density from the baseline value have almost no impact on the computed heat transfer. Based on these results, the baseline grid just described was determined sufficient to provide grid resolved solutions to within 5%. A separate resolution study was not performed at all trajectory points; it is assumed this grid density would be sufficient for the remaining (lower Reynolds number) solutions. All cases have the same surface grid, but the outer boundary is tailored for each case to ensure that the grid is well aligned to the bow shock and flow features.

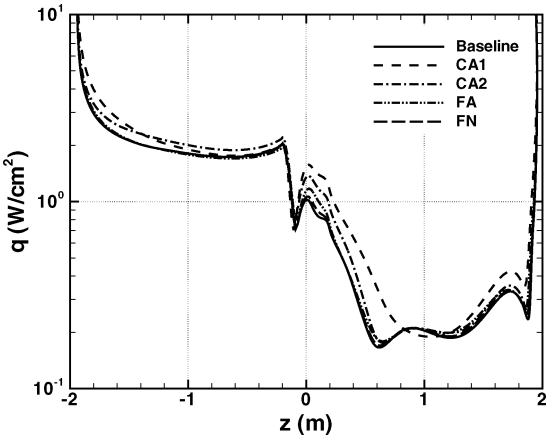

Fig. 5 Computed heat transfer on the afterbody in the symmetry plane at $t = 4510$ s, showing the effects of grid refinement in the streamwise and normal directions. The windward (attached) side is in the negative z direction; $z = 0$ is the rear apex.

B. Wake Structure and Surface Features

Examination of the wake structure for this type of flow is necessary to understand the resultant surface heating. An instructive first step is to examine flow structures in the pitch plane. Figure 6 shows the pitch plane streamlines colored by the local translational temperature for five selected trajectory points: $t = 4510$, 4600, 4700, 4800, and 4900 s. The solutions in Fig. 6 span more than an order of magnitude in freestream Reynolds number, ranging from $Re_D = 4.3 \times 10^4$ at $t = 4700$ s to $Re_D = 7.6 \times 10^5$ at $t = 4900$ s. In all cases the flow remains attached on the windward side of the conical afterbody, in contrast to preflight expectations.[9] Separation occurs near the maximum diameter point on the shoulder on the lee side.

For all five cases, a critical point[39] (shown as a red dot) is apparent in the near wake on the lee side. Figure 6f shows the locations of the critical point for the five cases. The location of this critical point depends on the freestream Mach and Reynolds numbers and the angle of attack. For the present set of computations, the angle of attack does not vary more than ± 0.4 deg about an average value of 18.2 deg, and the any dependence of the critical point location on the angle of attack is unlikely to be seen. It is evident from Fig. 6f that the critical point moves away from the surface with decreasing Reynolds number. However, the axial x location seems to be constant between $t = 4510$ and $t = 4800$ s, where the Mach number ranges from 25.6 to 20.5. This suggests that the Mach number has a weaker influence on the axial location of the critical point. However, at $t = 4900$ s, where the Reynolds number is the highest, and the Mach number the lowest in selected set of points, the critical point moves further upstream on the leeward side. This movement is a combined influence of both the freestream Mach and Reynolds numbers, which is complicated by the fact that neither is monotonic in time because of the skip maneuver.

The computed oil flow patterns (surface streamlines) on the afterbody are shown in Fig. 7 for the same trajectory points as in Fig. 6. The oil flow patterns represent the direction of the surface shear stress. As is typical for separated laminar flows, the size of the separation region increases with Reynolds number (see Fig. 7, which shows similar structures and patterns). At the highest

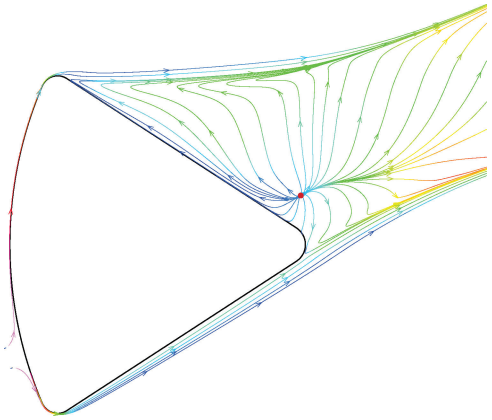

a) $t = 4510$ s, $M_\infty = 25.6$, $Re_D = 3.2 \times 10^5$, and $\alpha = 17.8$ deg

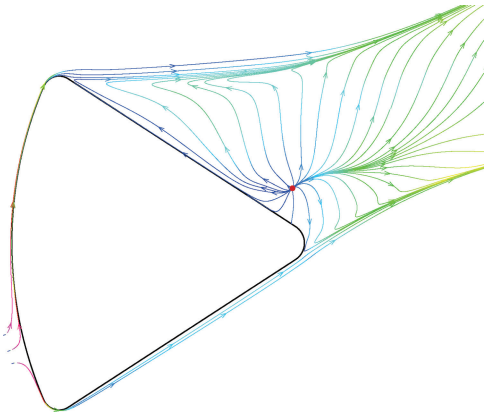

d) $t = 4800$ s, $M_\infty = 20.5$, $Re_D = 2.1 \times 10^5$, and $\alpha = 18.4$ deg

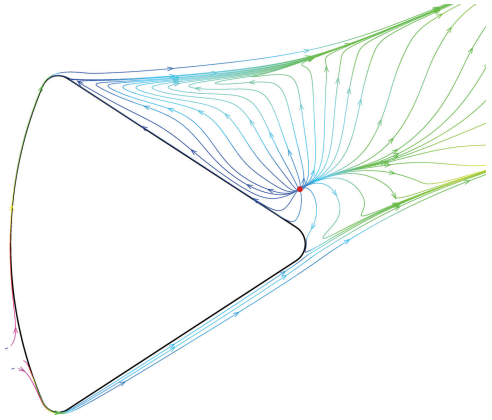

b) $t = 4600$ s, $M_\infty = 22.9$, $Re_D = 1.3 \times 10^5$, and $\alpha = 18.3$ deg

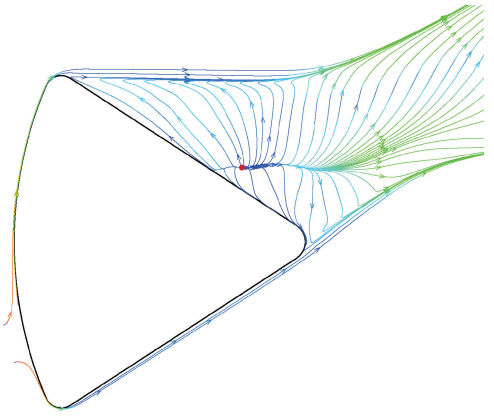

e) $t = 4900$ s, $M_\infty = 13.2$, $Re_D = 7.6 \times 10^5$, and $\alpha = 18.6$ deg

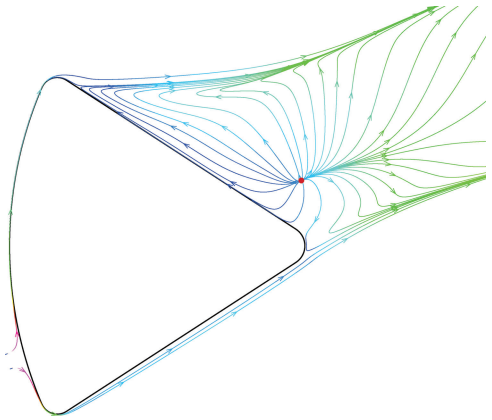

c) $t = 4700$ s, $M_\infty = 22.7$, $Re_D = 4.3 \times 10^4$, and $\alpha = 18.5$ deg

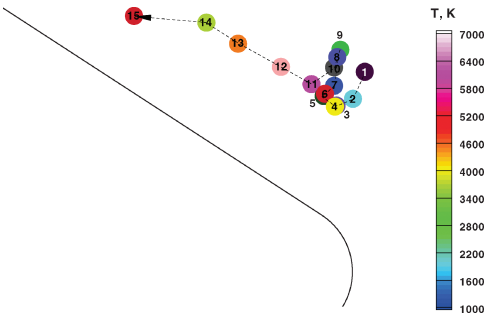

f) Critical point movement

Fig. 6 Streamlines colored by translational temperature in the pitch plane for five trajectory points between $t = 4510$ and 4900 s, and critical point location for all 15 solutions.

Reynolds number ($t = 4900$ s), the surface oil flow pattern is very different from the others. However, for this case the computed flowfield is unsteady and the present computations, which are not time accurate, cannot adequately capture the unsteadiness. The oil flow patterns in Fig. 7 are superimposed over the radiative equilibrium surface temperature contours (shown on a local scale of 200–1200 K relevant to the afterbody). The location of the critical points (such as nodes, foci, saddle points) on the surface are indicated as blue dots on the port side of the vehicle. The richness and complexity of the flow is evident from the figures. Further, the separation lines and change in surface temperature across them are clearly seen. The areas of locally increased temperature are seen at the nodes/foci. These local hot spots correspond to vortex impingement on the surface. Local maxima in surface temperature also occur at the rear apex for all cases.

In addition to the flow structures in the pitch plane and the vehicle surface, one can also examine the three-dimensional flow behind the vehicle. Although the interactive use of flow-visualization software provides much more information than static images, an attempt at presenting the nature of the wake flow is made in Fig. 8 for three trajectory points: $t = 4510$, 4600, and 4900 s. Each figure shows the sonic surface envelope around the vehicle, along with vortex cores and volume streamtraces in the wake. Also shown are contours of axial velocity (Cartesian component u) on three slices through the volume at $x = 4$, 7, and 10 m. The decrease in the extent of the sonic surface with decreasing Mach number is evident

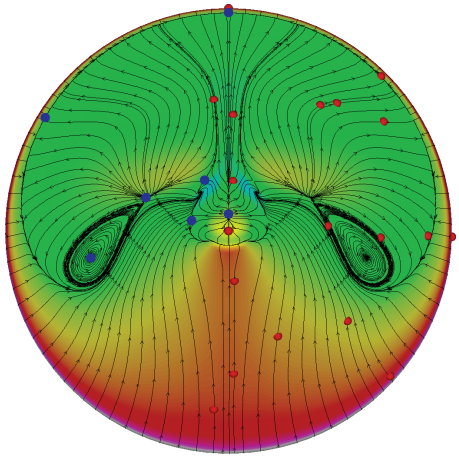

a) $t = 4510$ s, $M_\infty = 25.6$, $Re_D = 3.2 \times 10^5$, and $\alpha = 17.8$ deg

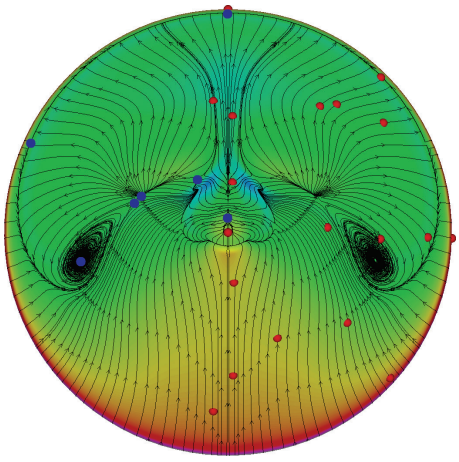

d) $t = 4800$ s, $M_\infty = 20.5$, $Re_D = 2.1 \times 10^5$, and $\alpha = 18.4$ deg

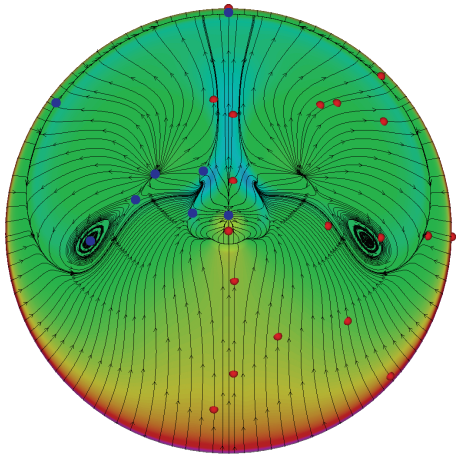

b) $t = 4600$ s, $M_\infty = 22.9$, $Re_D = 1.3 \times 10^5$, and $\alpha = 18.3$ deg

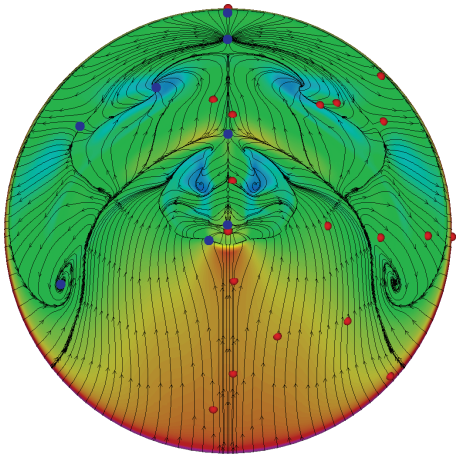

e) $t = 4900$ s, $M_\infty = 13.2$, $Re_D = 7.6 \times 10^5$, and $\alpha = 18.6$ deg

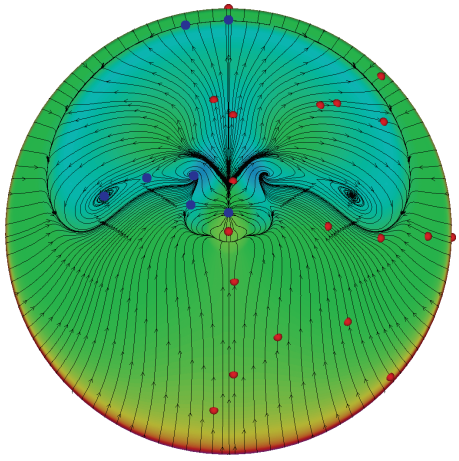

c) $t = 4700$ s, $M_\infty = 22.7$, $Re_D = 4.3 \times 10^4$, and $\alpha = 18.5$ deg

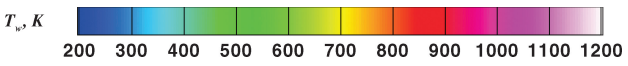

Fig. 7 Oil flow patterns on the afterbody for five trajectory points between $t = 4510$ and 4900 s. Surface colored by radiative equilibrium temperature ($\varepsilon = 0.85$). The calorimeter locations are indicated by red dots, and the critical points are indicated by blue dots.

from the figure. The usual practice of examining the sonic region in the pitch plane to determine wake closure could be very misleading. Because of the crossflow induced by the angle of attack, the sonic surface develops two lobes corresponding to the off-axis trailing vortices, and this twin-lobed sonic surface extends much further aft in regions away from the pitch plane as these vortices separate in the wake. The characteristic rotational structure of the afterbody flow is clearly brought out through the volume stream traces contained in the subsonic volume in the afterbody region. The vortex cores, extracted using Tecplot® (Ref. 40), are indicated as solid red lines in the figures. There are two large counter-rotating vortices on the leeside, and two more below these past the rear apex. The footprints of the four-vortex system are clearly seen in the axial slices through the volume. The separation between the upper and lower vortex system increases with decreasing Mach number.

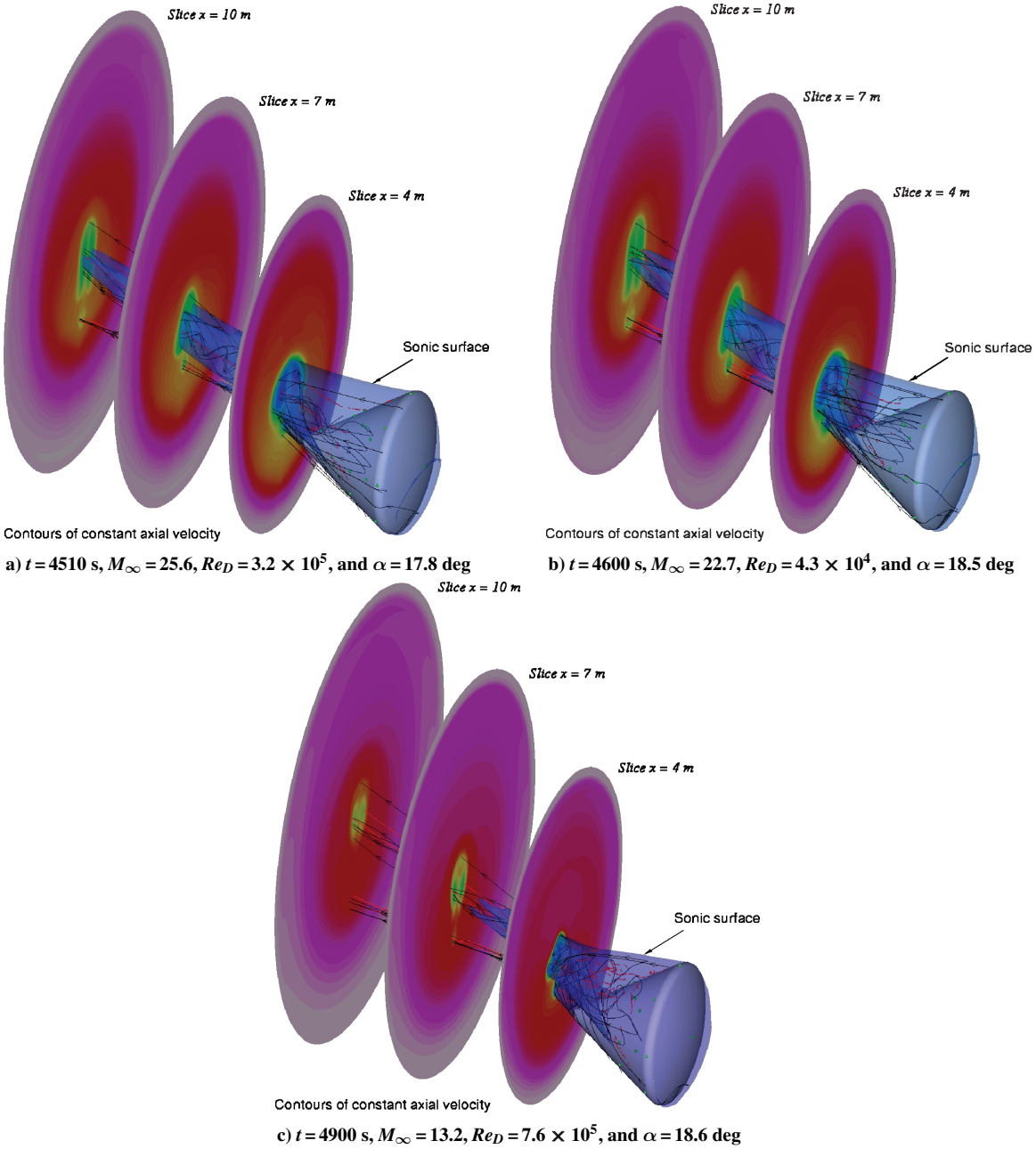

Fig. 8 Three-dimensional wake flow structure from computations at three trajectory points. The translucent envelope around the vehicle is the sonic surface. The three planes aft of the vehicle are slices through the volume taken at $x = 4$, 7, and 10 m. The slices are painted with contours of axial velocity (Cartesian component u). The solid red lines are the vortex cores extracted from the volume solutions.

C. Comparisons to Experimental Data

Figure 9 shows the comparison between the computed afterbody heat transfer and the experimental data for each of the 19 functional calorimeters on the AS-202 command module. The agreement between the computations and the data is generally within the assumed experimental uncertainty for 15 of the 19 calorimeters. The calorimeters will be discussed in four separate groups: those on the shoulder in attached flow (h and i) those on the windward (attached) side of the afterbody (a–d, f, and g), those in the separated flow region (e, m, and o–s), and those near the separation line (j, k, l, and n).

On each plot in Fig. 9, the flight data, which were scanned from Ref. 9, are shown as crosses. At some locations, particularly during the second heat pulse, there were multiple signal spikes. For example, notice the sharp heating spikes in the flight data on Fig. 9l at around $t = 4460$ and 4900 s. These spikes were determined by Lee et al.[9] to correspond to the times of RCS firings and thus are considered to be spurious. The data points that are estimated by the present authors to be spurious are shown on the plots as open circles. The best fit to the data for each case is then obtained using a Fourier-function-based least-squares fitting procedure neglecting the spurious data points. Dashed lines indicate the estimated ±20% uncertainty about this best-fit line, as discussed in the Flight Instrumentation section. For the purposes of this work, the uncertainty is assumed to remain constant throughout the entry. Examination of Fig. 9 indicates that the assumed uncertainty encompasses the majority of the data scatter, with the exception of some of the calorimeters in the separated flow region, which have more scatter during the skip maneuver ($t = 4600$ to 4800 s). Finally, the CFD results at the 15 trajectory points are shown as diamonds connected by a solid line.

1. *Shoulder Region*

Two calorimeters were placed on the shoulder just before the maximum diameter point. Calorimeter h was placed midway between

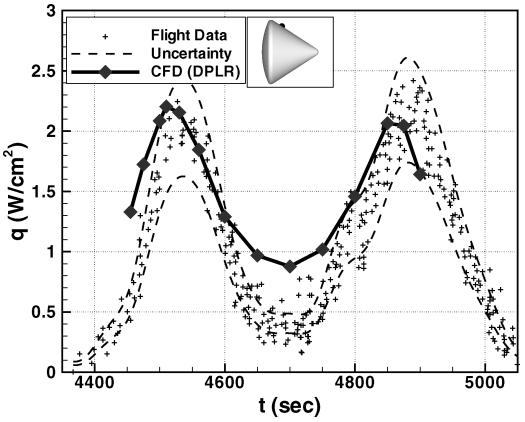

a) Calorimeter *a*

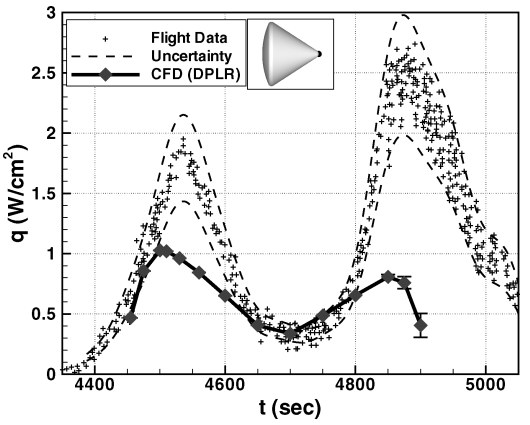

e) Calorimeter *e*

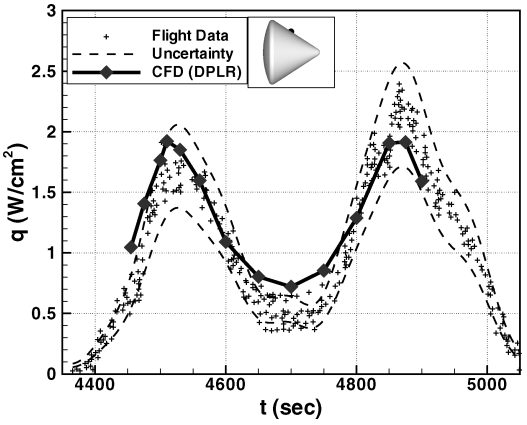

b) Calorimeter *b*

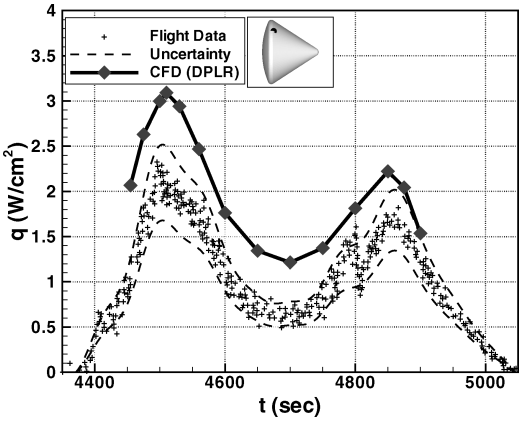

f) Calorimeter *f*

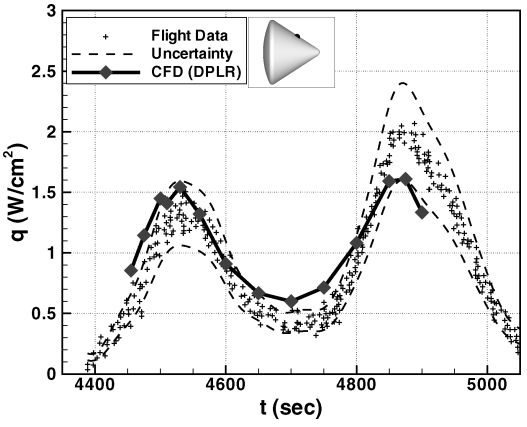

c) Calorimeter *c*

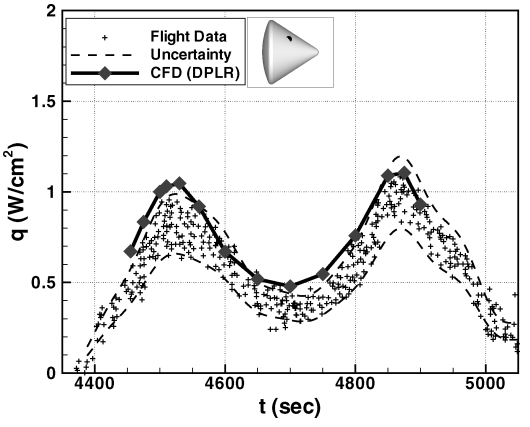

g) Calorimeter *g*

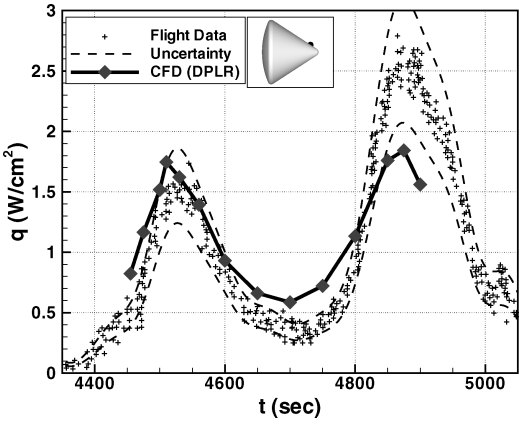

d) Calorimeter *d*

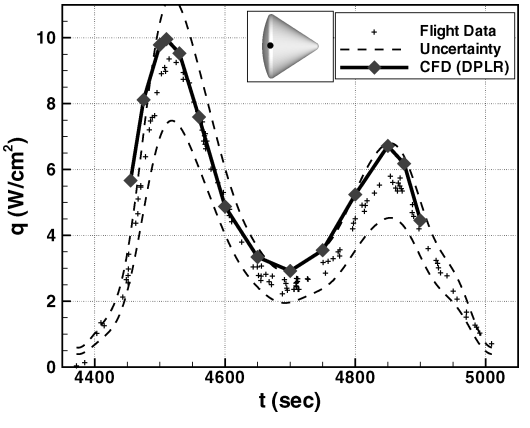

h) Calorimeter *h*

Fig. 9 Comparison of computed and experimental heat transfer for AS-202. Letters indicate calorimeter ID in Table 2.

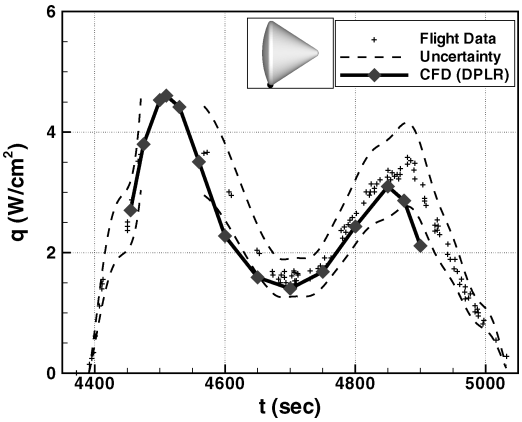

i) Calorimeter *i*

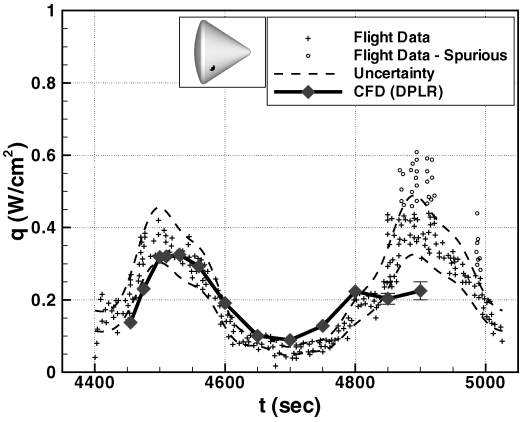

m) Calorimeter *m*

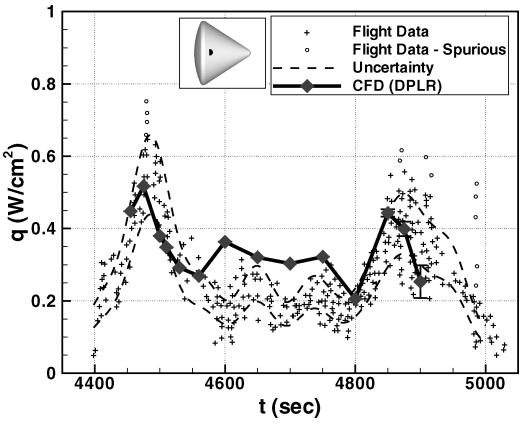

j) Calorimeter *j*

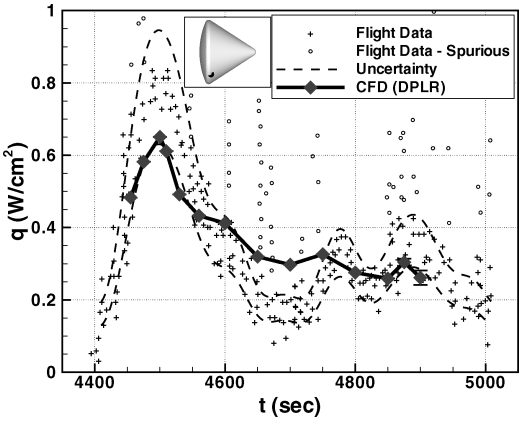

n) Calorimeter *n*

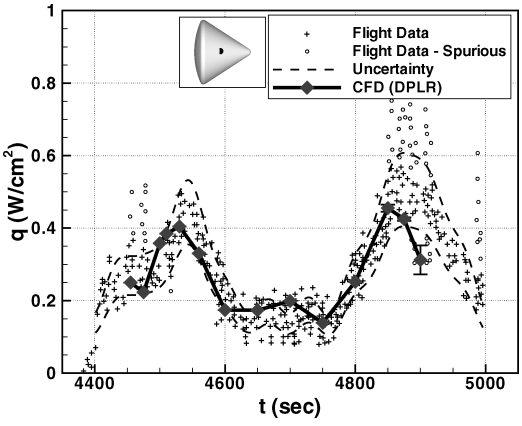

k) Calorimeter *k*

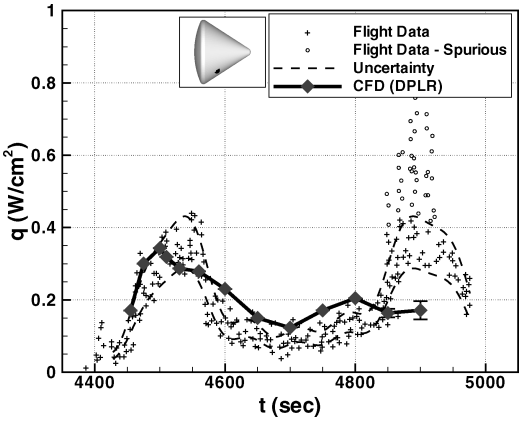

o) Calorimeter *o*

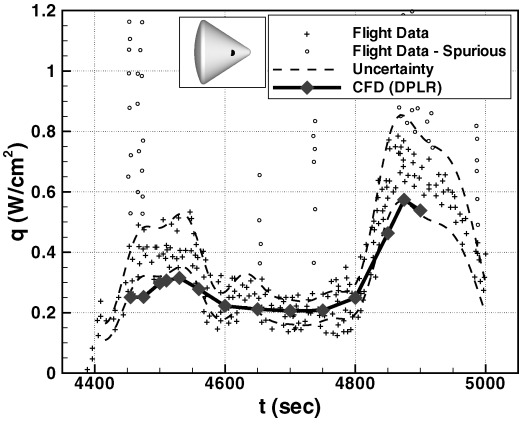

l) Calorimeter *l*

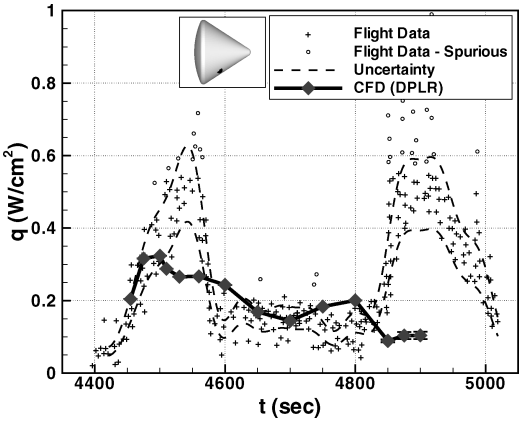

p) Calorimeter *p*

Fig. 9 Comparison of computed and experimental heat transfer for AS-202. Letters indicate calorimeter ID in Table 2 (continued).

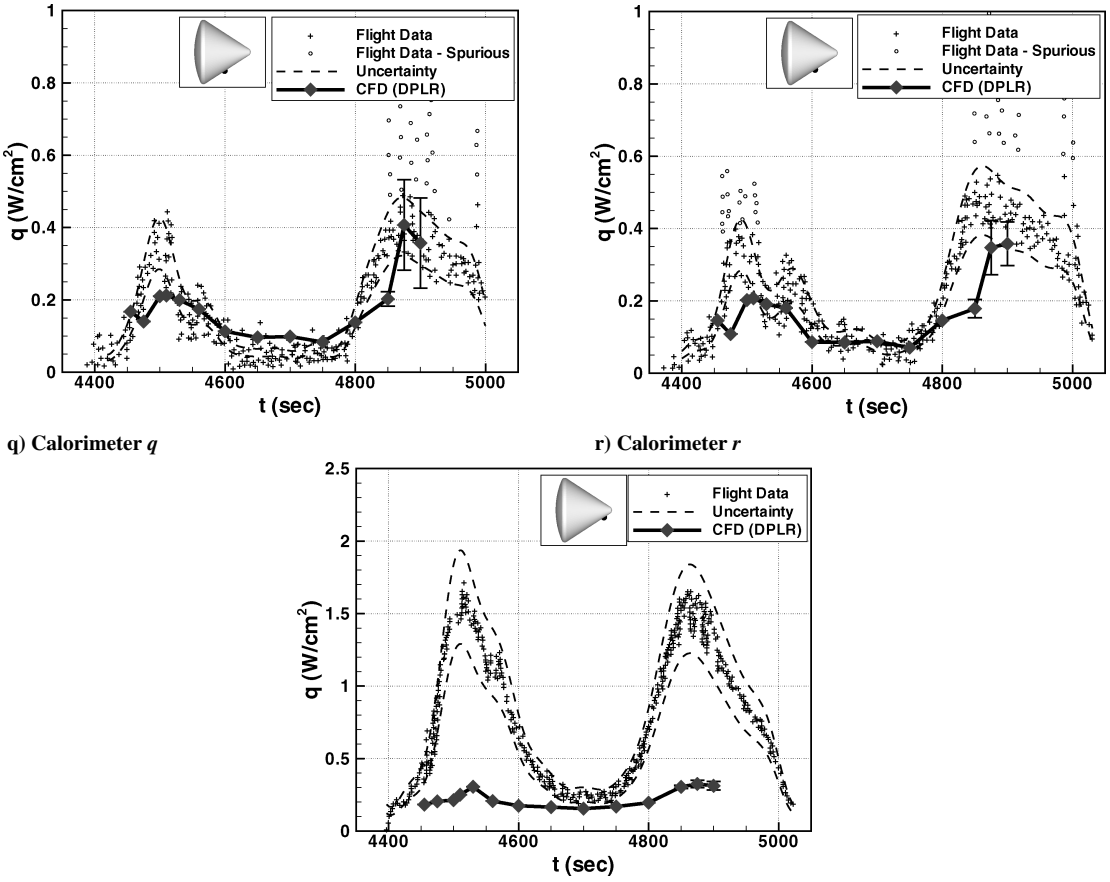

q) Calorimeter *q*

r) Calorimeter *r*

s) Calorimeter *s*

Fig. 9 Comparison of computed and experimental heat transfer for AS-202. Letters indicate calorimeter ID in Table 2 (continued).

the windward and leeward centerline ($\theta = 178.5$ deg), and i was placed on the leeward centerline ($\theta = 270$ deg). Figure 9h shows the comparison between the computed heating levels and the flight data for calorimeter h. The agreement between the CFD and flight data is good. The peak heat flux predicted by the CFD is about 10 W/cm^2 at $t = 4510$ s or about 6% higher than the flight data (9.4 W/cm^2). The agreement is generally within 20% over the entire trajectory, with the largest discrepancy occurring near the minimum between the two heat pulses ($t \sim 4700$ s).

The comparison for calorimeter i on the lee centerline is shown in Fig. 9i. Once again the agreement is within the assumed $\pm 20\%$ uncertainty throughout most of the flight. Note that calorimeter i apparently saturated above 3.7 W/cm^2, and thus no data were obtained during the peak of the first heat pulse. However, the trends predicted by the CFD before and after this loss of signal are in good agreement with the flight data, although the sparsity of flight data between 4560 and 4700 s make comparison difficult. The good agreement between the flight data and the CFD for these shoulder-mounted calorimeters is somewhat surprising, given the size of the lateral gradient in heat flux at this location.

2. *Attached Flow Region*

Six calorimeters were placed on the conical afterbody on the windward side in a region where the flow remained attached throughout the entry. Calorimeters *a–d* were placed on or near the windward centerline, as shown in Fig. 3. Calorimeter g was placed approximately midway between the shoulder and rear apex, at $\theta = 143$ deg. The comparisons between the computed and experimental heat flux for these calorimeters are shown in Figs. 9a–9d and 9g. From the figures we see that the agreement is generally good during the first heat pulse. The heating levels near the peak heating point ($t = 4510$ s) are predicted to within 10% at all locations. Computed heating levels during the early portion of the second heat pulse also agree well with flight data, although the CFD results for calorimeters c and d at the final two trajectory points ($t = 4850$ and 4900 s) are lower than the flight data. The difference between the computation and flight data appears to increase with distance from the shoulder (the CFD results for calorimeter c are about 23% below the flight data at $t = 4900$ s, whereas those for calorimeter d underpredict flight data by 30%). This can indicate that the flowfield is transitioning to turbulence on the attached afterbody during the second heat pulse. This possibility will be examined in a later section.

The computed heating at these calorimeters overpredicts the flight heating near the trough between the heat pulses, with the amount of overprediction near $t = 4700$ s ranging from over 100% at calorimeter a to about 26% at calorimeter g. There are several possible reasons for the CFD to predict higher heating than was measured during flight during this time period. As discussed earlier, during the period between about 4600 and 4800 s the spacecraft was undergoing a skip maneuver that resulted in a local maximum in altitude at about 4700 s. During this skip phase, local areas of noncontinuum flow might have been present on the afterbody, which could result in an overprediction in heating. This possibility will be examined later in the paper. Another possibility arises from examination of the flight aerodynamic data in Hillje.[15] During the high-altitude skip phase of the entry, the uncertainty in vehicle orientation was much larger than average. In fact, between 4650 and 4750 s the uncertainty in angle of attack was approximately ± 2 deg, as opposed to ± 0.5 deg during the remainder of the entry. It is possible that the low dynamic pressure during this portion of the trajectory could have prevented the vehicle from maintaining its trim orientation, resulting in a slightly smaller than expected angle of attack. If the angle of attack were small enough, the flow could separate on the lee side of the afterbody, significantly reducing the predicted heating. To test this theory, a single run was made at $t = 4700$ s with an angle

of attack of 16.5 deg (2 deg less than nominal). The wind-side afterbody flow remained-attached for this case, and the resulting heat transfer at calorimeters *a–d* was about 15% lower. Although trend is certainly in the right direction, these results indicate that angle of attack alone cannot account for the differences in this portion of the trajectory.

Calorimeter *f* (Fig. 9f) was placed near the rear of the shoulder at $\theta = 138$ deg. For this calorimeter, the CFD predictions are uniformly 33–50% higher than the data. Given the level of agreement seen for the other five calorimeters in this region, as well as that seen for the two calorimeters on the shoulder, the reasons for this disagreement are not clear.

Finally, calorimeter *a* was at a location downstream of the windward scimitar antenna (see Fig. 3), which is not modeled in the current simulations. However, given the level of agreement between the computations and the flight data for this calorimeter, it seems reasonable to assume that the effect of this antenna on heating levels in this area was small.

3. Separated Flow Region

Seven calorimeters were placed in a region for which the flow remained separated during the entire heating portion of the entry. Computational results for five of these, calorimeters *m* and *o*−*r*, are in generally good agreement with the flight data (see Figs. 9m and 9o–9r). At each of these locations, the peak heat flux during each pulse was between 0.2–0.4 W/cm^2. Agreement between the simulation and flight data was generally within 15% during the first heat pulse and the trough between the pulses. In contrast, the CFD prediction was generally lower than the flight data during the second heat pulse, which could be a consequence of turbulent transition. Note that the computed flow in the separation region became unsteady after $t = 4850$ s. Therefore the computational results for 4850, 4875, and 4900 s include "error" bars, which attempt to bound the unsteadiness of the computed heat transfer.

The results for calorimeter *p* require further discussion. This calorimeter is located in close proximity to *o* (see Fig. 3), and the computational results predict very similar heat fluxes for each. In contrast the flight data indicate that the peak heating levels at calorimeter *p* were significantly higher than those at *o*. As a result, the CFD underpredicts the heating at calorimeter *p* by about 45% at $t = 4530$ s, whereas the prediction at calorimeter *o* is well within the data scatter. This apparent discrepancy can be explained by examination of the afterbody layout in Ref. 9. Whereas calorimeter *o* is mounted on a smooth area of the heat shield, calorimeter *p* was placed immediately in front of one of the rendezvous windows. Therefore, it seems likely that the window created a local flow disturbance that affected the heat flux measured by calorimeter *p*.

Calorimeter *e* was placed at the rear apex of the aeroshell. As seen in Fig. 9e, the computations agree well with the flight data early in the first heat pulse and during the trough, but the computations significantly underpredict the peak heating levels. At $t = 4530$ s the CFD result is about 45% lower than the flight data indicate. The disagreement during the second heat pulse can possibly be caused by turbulent transition, but the differences in the first pulse are more difficult to understand. One possibility is that the local geometry of the apex is not accurately modeled in the current simulations.

By far the poorest agreement between the flight data and the CFD occurs at calorimeter *s* (Fig. 9s), which is near the rear apex on the leeward side near the centerline. At this location the flight data indicates heating levels nearly as high as those at the apex (calorimeter *e*), and slightly higher than those observed at calorimeter *d*, which was at the same *x* location but near the windward centerline. The computations predict very low heating levels at this location, consistent with those in the rest of the separated flow region. The reasons for this disagreement are not clear. Physically, the apex should create a separated flow region immediately behind it that would result in significantly lower heat transfer at calorimeter *s* than either *e* or *d*, unless a local vortex structure were generated that is not predicted in the CFD solutions. One possible explanation is that the nonzero sideslip angle significantly altered the flow patterns in this region; this effect will be explored in the following section. Unfortunately, calorimeter *s* was not functional on flight AS-201,[9] and a different instrumentation layout was used during Apollo 4 and 6,[10] so that it is not possible to use data from those flights to help determine whether the readings from AS-202 are spurious or indicative of a shortcoming in the current simulations.

4. Separation Line Region

Four calorimeters were placed in locations that were very near the separation line. Because the separation point is a function of Reynolds number, these calorimeters were in attached flow during a portion of the trajectory and separated flow during the remainder. The agreement between the computations and the flight data for these calorimeters is also generally good throughout the entry, as seen in Figs. 9j–9l and 9n. The clearest evidence of transition from attached to separated flow can be seen at calorimeter *j*, where the CFD shows sudden jumps in computed heating between $t = 4560$ and 4600 s and again between $t = 4750$ and 4800 s as the flow at this location attaches and then separates again. Similar jumps can be seen in the raw flight data at this location around $t = 4600$ and 4750 s (see Fig. 9j), although the levels are 20–30% lower than that predicted by the CFD. The computation also shows a jump in heating at calorimeter *k* at $t = 4700$ s that corresponds to a transition from separated to attached flow. However in this case the scatter makes it impossible to determine whether a corresponding event was seen during the flight. Transition from a separated to an attached flow state is not readily visible in the surface heating at the other two calorimeter locations; however, the general good agreement between the computations and the flight data indicates that the extent of separation is accurately predicted in the current simulations.

D. Surface Boundary Conditions

As discussed in the Flight Instrumentation section, the calorimeter surface might have a lower emissivity than the Avcoat TPS material. To quantify the impact of this emissivity difference on the results, a solution is run at $t = 4510$ s with a surface emissivity of 0.15 rather than the value of 0.85 assumed for the TPS. Figure 10a shows the comparison of computed centerline heating on the afterbody for these two cases. From the figure we see that, as expected at these heating levels, surface emissivity has only a small impact on the computed heat transfer. The largest effect occurs on the leeward side of the apex, where the lower emissivity increases the heat transfer by about 15%. The predicted heat transfer was within 10% over the rest of the surface. Similar results are expected at the other trajectory points.

In contrast, the computed heat transfer is very sensitive to the wall catalysis model employed. As stated earlier, the carbonaceous Avcoat TPS material should have a high catalycity. However, to bound the influence of catalytic heating on the total heat flux, a solution is run at $t = 4510$ s assuming a noncatalytic surface. As shown in Fig. 10b, the assumption of a noncatalytic surface reduces the predicted heating rate by a factor of 3 to 4 over the entire afterbody. Given the level of agreement between the flight data and the fully catalytic results, it is clear that a fully catalytic surface assumption is indeed warranted for the Avcoat material.

E. Sideslip Effects

All computations presented thus far assumed zero sideslip (yaw). However, the flight data indicated that a small sideslip angle was indeed present during the majority of the entry (see Table 3).[15] To assess the impact of yaw on the computed heating, a single case is run at $t = 4500$ s, which includes the measured sideslip angle ($\beta = 2.5$ deg). The grid for this case is constructed by mirroring the baseline grid to generate a full 360-deg revolution and then tailoring the outer boundary to the correct (asymmetric) shock location using SAGe.[38] The resulting grid has approximately three million points. Figure 11 shows computed heating on the afterbody at $t = 4500$ s with and without yaw included in the simulation. The two images look qualitatively similar except for the expected "tilt" in the heating distribution for the case with sideslip. The most noticeable differences are in the relative magnitude of heating at the two vortex

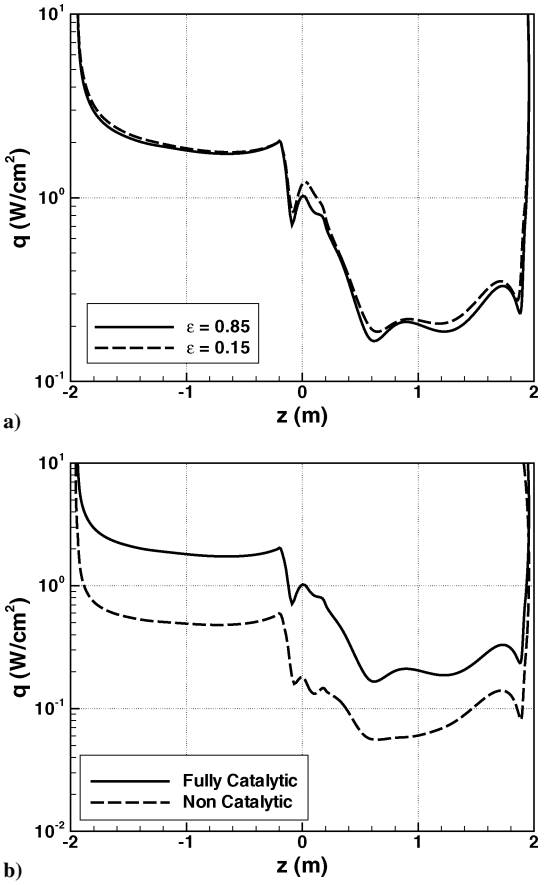

Fig. 10 Impact of a) surface emissivity and b) surface catalycity on computed afterbody heat transfer along the vehicle centerline at $t = 4510$ s.

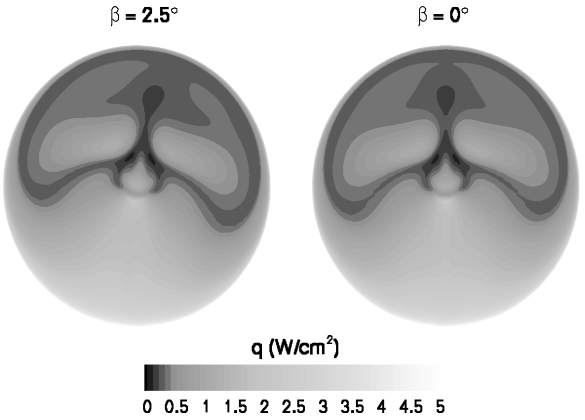

Fig. 11 Impact of 2.5-deg sideslip angle on computed afterbody surface heat transfer at $t = 4500$ s.

impingement points and the location of the cool streak down the leeward centerline. Based on Fig. 11, it would seem that the impact of sideslip on computed heating at most calorimeter locations would not be large, and this is in fact the case. A positive 2.5-deg sideslip angle changes the predicted surface heating by more than 10% for only four of the 19 functional calorimeters. The most notable differences in the attached flow region occur at calorimeters f and h, where a positive yaw causes a decrease in heating of about 14%, bringing the computations at both locations in better agreement with flight data. In the separated flow region the positive yaw angle results in a 20% increase in predicted heating at calorimeters q and r, again resulting in better agreement with flight data. Interestingly the sideslip angle has essentially no effect on the predicted heating at calorimeters e and s, indicating that sideslip is not the cause of the disagreement between the computations and flight data at these locations.

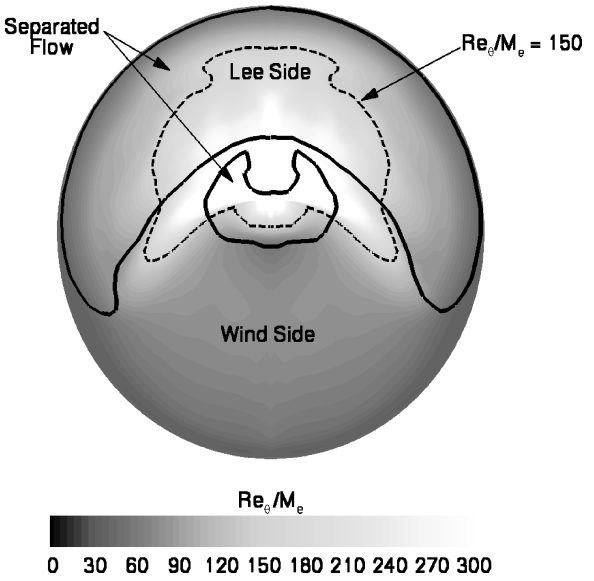

Fig. 12 Computed transition parameter Re_θ/M_e on the conical afterbody for $t = 4900$ s.

F. Transition to Turbulence

All of the calculations shown to this point have been performed assuming that the entire flowfield was laminar. Given the low freestream Reynolds numbers (see Table 3), particularly during the first heat pulse, this assumption should be reasonable; nevertheless, the possibility of turbulent transition will be considered separately for the attached portion of the afterbody flow and the separated flow region.

Postflight data analysis, based on the assumption that the flow was separated on the entire afterbody, seemed to indicate a transition to turbulence soon after the skip maneuver was complete ($t > 4800$ s) (Ref. 9). However, the current results show that the flow remains attached on the wind side, and that a laminar flow assumption accurately predicts windward heating levels during most of the second heat pulse. To evaluate the likelihood of transition in the attached afterbody flow, we use the standard correlation $Re_\theta/M_e > \text{const}$,[41] where Re_θ is the momentum thickness Reynolds number and M_e is the (supersonic) edge Mach number. The constant varies between approximately 150 and 350 depending on the roughness characteristics of the surface. This quantity is computed on the surface for all trajectory points; the results for the case with the highest freestream Reynolds number ($t = 4900$ s) are shown in Fig. 12. The black lines in the figure denote the separation and attachments lines of the complex wake (see Fig. 6). From Fig. 12 we see that Re_θ never exceeds 150 in the attached flow portion on the wind side of the afterbody, indicating that the majority of the attached flow will remain laminar. Note that the high values of Re_θ/M_e in and near the separated flow region are not necessarily indicative of turbulence because this criterion relies on accurate detection of the boundary-layer edge, something that is difficult to do in a wake flow. This conclusion is consistent with the current analysis, although there is some evidence in the heating data of transition near $t = 4900$ s at calorimeters c and d. To evaluate the impact of turbulent flow on the afterbody, a fully turbulent solution is computed at $t = 4900$ s using Menter's SST model.[35] The computed turbulent heating levels are 3.3 W/cm^2 at calorimeter c and 3.2 W/cm^2 at calorimeter d, as compared to the laminar computed values of 1.3 and 1.6 W/cm^2 and the flight data of and 1.8 and 2.4 W/cm^2, respectively. This suggests that although it is possible that the flow was transitional on this part of the body, a fully developed turbulent boundary layer was not established until later in the flight.

To estimate the likelihood of transition in the separated flow region, we use the blunt-body separation shear-layer correlation given by Lees.[42] This correlation is given by $Re_{\text{tr}} = \rho_e V_e L/\mu_e$, where ρ_e, V_e, and μ_e are the density, velocity, and viscosity, respectively, at the outer edge of the separation shear layer, and L is the laminar running

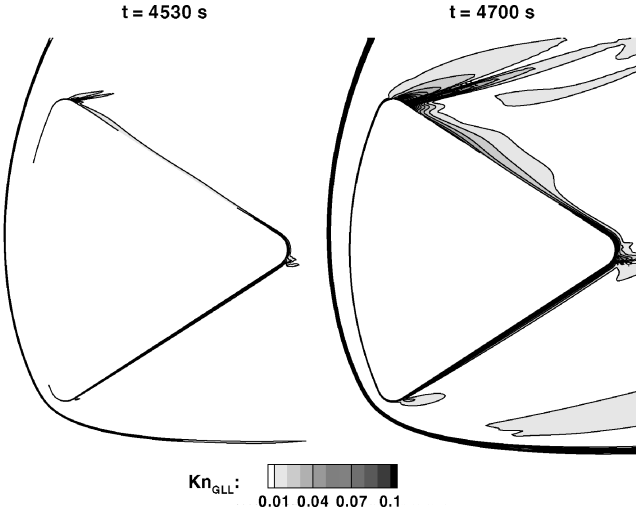

Fig. 13 Contours of continuum breakdown parameter Kn_{GLL} in symmetry plane for $t = 4530$ and 4700 s.

length. According to Lees,[42] the local transition Reynolds number ranges from about 3×10^4 to 2×10^5 for edge Mach numbers between 2 and 4. This quantity was evaluated for several trajectory points, and it was determined that the separated flow region would likely remain laminar until $t = 4900$ s, at which point the lee-side shear layer reaches a local Reynolds number within a factor of two of the critical value. Based on these results it appears that the assumption of laminar flow is valid in the separation region for the majority of the time period examined in this work. However, the correlation of Lees is for axisymmetric flows. It is possible that three-dimensional (crossflow) effects could hasten transition to turbulence for this case.

G. Noncontinuum Flow Effects

All solutions in this work are obtained assuming a continuum flow. However, at these Reynolds numbers, noncontinuum effects can be present in the base region. To assess the importance of noncontinuum effects on the computed heat transfer, the density gradient length local Knudsen number Kn_{GLL} (see Ref. 43) was computed for all cases. Following the work of Boyd et al.,[43] we assume that continuum breakdown will begin when $Kn_{GLL} > 0.05$. Figure 13 shows the resulting contours of Kn_{GLL} in the symmetry plane for $t = 4530$ and 4700 s. In the near-wall region these computations indicate that at $t = 4530$ s the entire afterbody with the exception of the wind side of the rear apex should be in continuum flow. At $t = 4700$ s, $Kn_{GLL} > 0.05$ on the entire wind side of the afterbody and becomes quite large near the rear apex and the shoulder region, indicating that noncontinuum effects are likely present. Interestingly, the near-wall continuum breakdown parameter is larger on the windward (attached) side of the frustum than in the separated flow region, because of the larger density gradients in the attached flow boundary layer. Although Boyd et al.[43] did not explicitly quantify the relationship between Kn_{GLL} and the computed heat transfer, in general, a Navier–Stokes solution will slightly overpredict heat transfer in the base region of a noncontinuum flow.[44] Given that Fig. 13 demonstrates a potential continuum breakdown near $t = 4700$ s and that this effect should be more pronounced in the attached afterbody flow, noncontinuum flow effects can well explain the overprediction in heating observed for calorimeters $a-d$ and g around this time.

VII. Conclusions

CFD simulations were performed to simulate the wake flow and afterbody heating environment of the Apollo AS-202 command module. The AS-202 mission entered the Earth's atmosphere at orbital velocities on a shallow flight-path angle that led to low afterbody heating levels, making data reduction straightforward and providing a good set of validation data for laminar flow on a lifting entry capsule. Fifteen three-dimensional simulations were performed, which covered the majority of the heating portion of the flight. The surface was assumed to be fully catalytic and in radiative equilibrium, which are appropriate assumptions for the Avcoat TPS material. The wake structure was examined, and surface oil flow plots demonstrated that the flow remained attached on the windward side of the afterbody throughout the entry. The computed heat transfer was well within the assumed $\pm 20\%$ uncertainty in the flight data for 15 of the 19 functional calorimeters on the conical afterbody over most of the flight. Heating was generally overpredicted on the windward side during the trough between the two heat pulses, possibly because of noncontinuum effects, and underpredicted on the windward side late in the second heat pulse, possibly because of transition to turbulence on the flight vehicle that was not modeled in the current simulations. Predicted heating at two calorimeters located near the separation line clearly show jumps where the flow separates and reattaches as a function of time. This behavior was also seen in the flight data. The worst agreement between the computations and the flight data occurred near the rear apex of the command module. The reasons for this disagreement are not known at this time, but might be partially caused by geometric differences between the apex as modeled in this work and the flight vehicle. The effects of sideslip were explored and found to be minor at all but four calorimeter locations.

The results presented in this work indicate that modern CFD methods are capable of predicting afterbody heating levels on a lifting Earth entry capsule in laminar flow and form a solid basis from which our ability to predict aeroheating in the presence of turbulence and ablation can be explored. Furthermore, although more work needs to be done to fully validate afterbody aeroheating predictions, the current results suggest that the large design uncertainties ($\sim 200\%$) commonly applied to such simulations are needlessly conservative.

Acknowledgments

This work was funded by the In-Space Propulsion program under task agreement M-ISP-03-18 to NASA Ames Research Center. The work performed by the second author was supported by the prime contract NAS2-99092 to ELORET Corporation. The authors would like to thank David Saunders (ELORET) for his help converting the raw experimental data into usable form, Ryan McDaniel (NASA Ames) for his ideas on grid generation, Bernard Laub (NASA Ames) for discussions on the properties of the Avcoat TPS material, and Gary Allen (ELORET) for his guidance in interpreting the aerodynamic and outer-mold-line data.

References

[1]Jones, R., "Experimental Investigation of the Overall Pressure Distribution, Flow Field, and Afterbody Heat Transfer Distribution of an Apollo Reentry Configuration at a Mach Number of 8," NASA TM X-813, June 1963.

[2]Bertin, J., "Wind Tunnel Heating Rates for the Apollo Spacecraft," NASA TM X-1033, Jan. 1965.

[3]Marvin, J., and Kussoy, M., "Experimental Investigation of the Flow Field and Heat Transfer over the Apollo Capsule Afterbody at a Mach Number of 20," NASA TM X-1032, Feb. 1965.

[4]Yee, L., "Free-Flight Measurements of Heat Transferred to the Apollo Afterbody with and Without Heat Shield Ablation," NASA TM X-1096, April 1965.

[5]Lee, G., and Sundell, R., "Apollo Afterbody Heat Transfer and Pressure with and Without Ablation at M_∞ of 5.8 to 8.3," NASA TN D-6792, April 1972.

[6]Fox, G., and Marvin, J., "An Investigation of the Apollo Afterbody Pressure and Heat Transfer at High Enthalpy," NASA TM X-11973, March 1966.

[7]Cauchon, D. L., "Project Fire Flight 1 Radiative Heating Experiment," NASA TM X-1222, April 1966.

[8]Cauchon, D. L., "Radiative Heating Results from the Fire II Flight Experiment at a Reentry Velocity of 11.4 Kilometers per Second," NASA TM X-1402, July 1967.

[9]Lee, D. B., Bertin, J. J., and Goodrich, W. D., "Heat Transfer Rate and Pressure Measurements Obtained During Apollo Orbital Entries," NASA TN D-6028, Oct. 1970.

[10]Lee, D. B., and Goodrich, W. D., "The Aerothermodynamic Environment of the Apollo Command Module During Superorbital Entry," NASA TN D-6792, April 1972.

[11]Lee, D. B., "Apollo Experience Report: Aerothermodynamics Evaluation," NASA TN D-6843, June 1972.

[12]Wright, M., Loomis, M., and Papadopoulos, P., "Aerothermal Analysis of the Project Fire II Afterbody Flow," *Journal of Thermophysics and Heat Transfer*, Vol. 17, No. 2, 2003, pp. 240–249.

[13]Henline, W., Chen, Y.-K., Palmer, G., and Stewart, D., "Trajectory-Based, 3-Dimensional Heating and Ablation Calculations for the Apollo Lunar/Earth Return Capsule," AIAA Paper 93-2788, July 1993.

[14]Park, C., "Stagnation-Point Radiation for Apollo 4," *Journal of Thermophysics and Heat Transfer*, Vol. 18, No. 3, 2004, pp. 349–357.

[15]Hillje, E., "Entry Flight Aerodynamics from Apollo Mission AS-202," NASA TN D-4185, Oct. 1967.

[16]Pavlosky, J. E., and St. Leger, L. G., "Apollo Experience Report: Thermal Protection Subsystem," NASA TN D-7564, Jan. 1974.

[17]Crouch, R. K., and Walberg, G. D., "An Investigation of Ablation Behavior of Avcoat 5026/39M over a Wide Range of Thermal Environments," NASA TM X-1778, April 1969.

[18]Gardon, R., "A Transducer for the Measurement of Heat Flow Rate," *Journal of Heat Transfer*, Vol. 82, Nov. 1960, pp. 396–398.

[19]"Standard Test Method for Measuring Heat Flux Using a Copper-Constantan Circular Foil, Heat-Flux Transducer," ASTM E511-01, American Society for Testing and Materials, West Conshocken, PA, Oct. 2001.

[20]Murthy, A. V., "Radiative Calibration of Heat-Flux Sensors at NIST: Facilities and Techniques," *Journal of Research of the National Institute of Standards and Technology*, Vol. 105, No. 2, 2000, pp. 229–300.

[21]Pitts, D., and Carter, P., "High Altitude Atmospheric Measurements for the Reentries of Gemini 6 and 7," NASA TM X-58003, Nov. 1966.

[22]Wright, M., Candler, G., and Bose, D., "Data-Parallel Line Relaxation Method for the Navier–Stokes Equations," *AIAA Journal*, Vol. 36, No. 9, 1998, pp. 1603–1609.

[23]MacCormack, R., and Candler, G., "The Solution of the Navier–Stokes Equations Using Gauss-Seidel Line Relaxation," *Computers and Fluids*, Vol. 17, No. 1, 1989, pp. 135–150.

[24]Yee, H., "A Class of High-Resolution Explicit and Implicit Shock Capturing Methods," NASA TM 101088, Feb. 1989.

[25]Jits, R., Wright, M. J., and Chen, Y.-K., "Application of a Closed-Loop Trajectory Simulation for TPS Design of Neptune Aerocapture Vehicle," *Journal of Spacecraft and Rockets*, Vol. 42, No. 6, 2005, pp. 1025–1034.

[26]Wright, M., Bose, D., and Olejniczak, J., "The Impact of Flowfield Radiation Coupling on Aeroheating for Titan Aerocapture," *Journal of Thermophysics and Heat Transfer*, Vol. 19, No. 1, 2005, pp. 17–27.

[27]Park, C., "Review of Chemical-Kinetic Problems of Future NASA Missions, I: Earth Entries," *Journal of Thermophysics and Heat Transfer*, Vol. 7, No. 3, 1993, pp. 385–398.

[28]Bose, D., and Candler, G., "Thermal Rate Constants of the N2 + O→ NO + N Reaction Using Ab Initio 3A" and 3A' Potential Energy Surfaces," *Journal of Chemical Physics*, Vol. 104, No. 8, 1996, pp. 2825–2833.

[29]Park, C., *Nonequilibrium Hypersonic Aerothermodynamics*, Wiley, New York, 1990, pp. 344–348.

[30]Millikan, R., and White, D., "Systematics of Vibrational Relaxation," *Journal of Chemical Physics*, Vol. 39, No. 12, 1963, pp. 3209–3213.

[31]Gupta, R., Yos, J., Thompson, R., and Lee, K., "A Review of Reaction Rates and Thermodynamic and Transport Properties for an 11-Species Air Model for Chemical and Thermal Nonequilibrium Calculations to 30000 K," NASA RP-1232, Aug. 1990.

[32]Palmer, G. E., and Wright, M. J., "A Comparison of Methods to Compute High Temperature Gas Viscosity," *Journal of Thermophysics and Heat Transfer*, Vol. 17, No. 2, 2003, pp. 232–239.

[33]Palmer, G. E., and Wright, M. J., "A Comparison of Methods to Compute High Temperature Gas Thermal Conductivity," AIAA Paper 2003-3913, June 2003.

[34]Ramshaw, J. D., "Self-Consistent Effective Binary Diffusion in Multicomponent Gas Mixtures," *Journal of Non-Equilibrium Thermodynamics*, Vol. 15, No. 3, 1990, pp. 295–300.

[35]Menter, F. R., "Two-Equation Eddy-Viscosity Turbulence Models for Engineering Applications," *AIAA Journal*, Vol. 32, No. 8, 1994, pp. 1598–1605.

[36]Brown, J. L., "Turbulence Model Validation for Hypersonic Flows," AIAA Paper 2002-3308, June 2002.

[37]Gnoffo, P., Price, J., and Braun, R., "Computation of Near Wake Aerobrake Flowfields," *Journal of Spacecraft and Rockets*, Vol. 29, No. 2, 1992, pp. 182–189.

[38]Davies, C., and Venkatapathy, E., "The Self Adaptive Grid Code SAGE, Version 3," NASA TM 208792, Aug. 1999.

[39]Tobak, M., and Peake, D. J., "Topology of Three-Dimensional Separated Flows," *Annual Review of Fluid Mechanics*, Vol. 14, 1982, pp. 61–85.

[40]"Tecplot® Version 10.0 User's Manual," Amtec Engineering, Inc., Bellevue, WA, 2002.

[41]Tauber, M. E., "A Review of High-Speed Convective Heat-Transfer Computation Methods," NASA TP-2914, July 1989.

[42]Lees, L., "Hypersonic Wakes and Trails," *AIAA Journal*, Vol. 2, No. 3, 1964, pp. 417–428.

[43]Boyd, I. D., Chen, G., and Candler, G. V., "Predicting Failure of the Continuum Fluid Equations in Transitional Hypersonic Flows," *Physics of Fluids*, Vol. 7, No. 1, 1995, pp. 210–219.

[44]Dogra, V. K., Moss, J. N., Wilmoth, R. G., Taylor, J. C., and Hassan, H. A., "Effects of Chemistry on Blunt Body Wake Structure," *AIAA Journal*, Vol. 33, No. 3, 1995, pp. 463–469.